# OMAE2021-61808

# A CFD APPROACH FOR MODELLING THE FLUID-STRUCTURE INTERACTION OF OFFSHORE AQUACULTURE CAGES AND WAVES

**Tobias Martin**[*]
Marine Civil Engineering
Department of Civil and Environmental Engineering
Norwegian University of Science and Technology
7491 Trondheim, Norway
Email: tobias.martin@ntnu.no

**Hans Bihs**
Marine Civil Engineering
Department of Civil and Environmental Engineering
Norwegian University of Science and Technology
7491 Trondheim, Norway

## ABSTRACT

*Open ocean aquaculture cages became recently a promising alternative to traditional fish cage designs. The offshore environment implies larger loads on the structures and higher risk of fish loss. Floating rigid aquaculture cages with stiff nets are considered as a possible solution to cope with these new challenges. Their design process requires more advanced tools to account for the non-linear fluid-structure interaction. This paper presents a suitable numerical approach for analysing the interaction of offshore aquaculture cages and waves using Computational Fluid Dynamics. Here, a numerical wave tank accounts for the accurate propagation of the waves, and structural dynamics solutions are utilised for the cage system. Two-way coupling is enabled by accounting for the influence of the net on the fluid. The numerical model is validated against measurements for the loads on and the responses of a mobile floating fish farm in waves and current.*

## INTRODUCTION

Traditional coastal aquaculture becomes less and less attractive due to its environmental impact on the surrounding marine environment. Open ocean aquaculture (OOA) is considered as a promising alternative today as it avoids near-coast restrictions and allows for the increase of the structural dimensions. Though, the relocation to offshore environments implies larger wave ac-

tion and current velocities acting on the structures as well as a higher risk of fish loss due to structural failure [1]. Amongst others, floating rigid structures with relatively stiff nets are considered as a promising solution for this new environment. The dimensioning of these type of systems requires advanced knowledge about the non-linear fluid-structure interaction involving the complex structural dynamics of the floater, mooring and nets as well as a non-linearly propagating free surface including extreme waves and wave-current interaction.

In the design process, experimental studies are typically conducted only for the final prototype due to cost restrictions. In addition, historical data from measurements of fixed net panels in current [2–4], flexible net panels in current [5], net cages in current [6] or net panels and cages in waves [7,8] are considered to design the nets. In contrast, numerical modelling represents a less expensive and more flexible way of determining the loads on different sub-modules and prototypes in the design phase. In the past, numerical methods for traditional aquaculture cages mostly relied on linear potential theory for the load calculation and empirical formulae for estimating the velocity reduction through the net [8, 9]. The existing numerical studies of OOA structures [10–12] used simplified methods to predict the structural deformations in linear waves. In order to accurately understand the impact of offshore conditions on the structural response, two-way coupled simulations are necessary. Here, the modelling of the hydrodynamic forces affecting the dynamics of the floating rigid structure, the net and the mooring system as well as their ef-

[*]Address all correspondence to this author.

fect on the surrounding fluid are necessary. Advanced numerical methods, such as computational fluid dynamics (CFD) models, are considered to be appropriate for investigating this non-linear interaction of fluid and structure in complicated conditions.

Chen and Christensen [13] were the first to publish a CFD approach for the fluid-structure interaction of fish cages and waves. It was based on the solution of the RANS equations in a two-dimensional numerical wave tank, a dynamic mesh algorithm for the floater and a lumped mass method to account for the deformation of the net. The coupling between net and fluid was accomplished using the porous medium approximation as given in [2, 5, 14–16]. This kind of approximation is necessary due to the large length scale difference between the twines of a net and the size of the complete structure, which prevents the resolution of the net on the same numerical grid as the fluid domain. The numerical model was tested against physical measurements of a two-dimensional floater with a net sheet attached. Even though a good agreement could be achieved, the applicability of the chosen approach is limited to mostly two-dimensional studies due to the porous medium approach [17]. Recently [18], a new CFD model was proposed to overcome this issue following a Lagrangian approach for the coupling of rigid [17] and flexible [19] net sheets and cages. It is based on the idea of continuous immersed boundary methods for fluid-structure interaction [20,21]. Here, an additional source term is included in the conservation law of momentum. The term accounts for the momentum loss of the fluid while passing the net and is calculated from the hydrodynamic loads on the net itself. The model was successfully validated for three-dimensional OOA structures in current.

The remaining work starts with an overview of the numerical framework in [18] with emphasise on the floating body algorithm and its new coupling to the motion of stiff nets. The model is then adopted to study the dynamic response of a floating rigid OOA structure in waves and current. Final remarks can be found at the end of the paper.

## NUMERICAL MODEL
### Fluid Dynamics
The two-way coupled solution for the fluid and floating body dynamics is described by the conservation equations of mass and momentum. In convective and one-fluid form, they can be expressed as

$$\nabla \cdot \mathbf{u} = 0, \tag{1}$$

$$\frac{\partial \mathbf{u}}{\partial t} + \mathbf{u} \cdot \nabla \mathbf{u} = -\frac{1}{\rho}\nabla p + \mathbf{g} + \mathbf{f} + \mathbf{S}, \tag{2}$$

with $\mathbf{u}$ the velocity vector, $p$ the pressure, $\mathbf{g}$ the gravitational acceleration vector, $\mathbf{f}$ the floating source term and $\mathbf{S}$ the coupling term for the net. In the fluid, (1)–(2) are the three-

dimensional Reynolds-averaged Navier-Stokes equations and continuity equation if the definition

$$\mathbf{f} = \nabla \cdot \left( \nu \left[ \nabla \mathbf{u} + \nabla \mathbf{u}^T \right] \right), \tag{3}$$

is used. In the solid phase, the term is defined such that a divergence free rigid body velocity field is ensured (see below).

The material properties, i.e. the density $\rho$ and the viscosity $\nu$, of the three phases air, water and solid are implicitly described using the zero level sets of signed distance functions (see Fig. 1). In the fluid domain, the level set function $\phi_f$ is transported in space and time using [22]

$$\frac{\partial \phi_f}{\partial t} + \mathbf{u} \cdot \nabla \phi_f = 0, \tag{4}$$

and reinitialised after each time step as proposed in [23]. In addition, the level set function $\phi_s$ is utilised to distinguish the solid from the fluid phase. Thus, the density and viscosity are defined as

$$\rho = \rho_s H(\phi_s) + (1 - H(\phi_s)) \cdot (\rho_w H(\phi_f) + \rho_a (1 - H(\phi_f))), \tag{5}$$

$$\nu = (1 - H(\phi_s)) \cdot (\nu_w H(\phi_f) + \nu_a (1 - H(\phi_f))), \tag{6}$$

with the indices $w$ for water, $a$ for air and $s$ for solid. The smoothed Heaviside step function

$$H(\phi) = \begin{cases} 0 & \text{if } \phi < -\varepsilon \\ \frac{1}{2}\left(1 + \frac{\phi}{\varepsilon} + \frac{1}{\pi}sin(\frac{\pi\phi}{\varepsilon})\right) & \text{if } |\phi| \leq \varepsilon \\ 1 & \text{if } \phi > \varepsilon, \end{cases} \tag{7}$$

is utilised to ensure a smooth transition between the different phases. Here, $\varepsilon = 2.1\Delta x$ and $\Delta x$ is the characteristic cell length. Turbulence effects are included as additional turbulent viscosity using the Boussinesq approximation and a modified $k$-$\omega$ turbulence model [24].

The set of equations (1) - (4) is solved on a staggered rectilinear grid using the finite difference method. The diffusion term in the fluid domain is discretised with a second-order accurate central difference in space and treated with the first-order Euler implicit method in time. Convection terms are discretised with fifth-order accurate weighted essentially non-oscillatory (WENO) schemes [25,26] adapted to rectilinear grids in space. All source terms are explicitly added to the equations. The pressure-velocity coupling is ensured by following an incremental pressure-correction algorithm [27] with the third-order
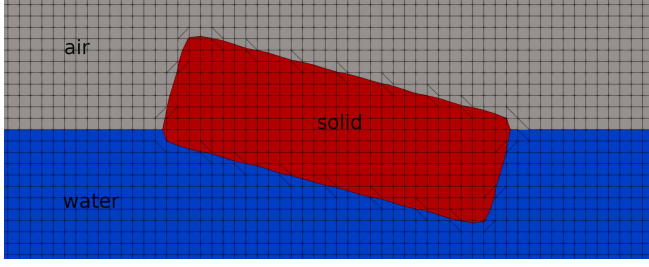
**FIGURE 1**: Illustration of the three phases in the computational domain. Water and air build together the fluid phase. The two interfaces between the phases are defined by the zero level sets of $\phi_f$ and $\phi_s$.

accurate TVD Runge-Kutta scheme [28] for the time discretisation. In each $k$-th sub-step of the Runge-Kutta scheme, a predictor step is applied to approximate the velocity field using the pressure gradients of the previous step:

$$\frac{\mathbf{u}^{(*)} - \alpha_k \mathbf{u}^{(n)}}{\alpha_k \Delta t} = \frac{\beta_k}{\alpha_k} \mathbf{u}^{(k-1)} - \mathbf{u}^{(k-1)} \cdot \nabla \mathbf{u}^{(k-1)} - \frac{\nabla p^{(k-1)}}{\rho}$$
$$+ \mathbf{f}^{(*)} + \mathbf{g} + \mathbf{S}, \tag{8}$$

with $\alpha_k = 1.0, 1/4, 2/3$, $\beta_k = 0.0, 3/4, 1/3$ and $k = 1, 2, 3$. The pressure and final velocity fields are then found as

$$p^{(k)} = p^{(k-1)} + p_{\text{corr}} - \rho \nu \, \nabla \cdot u^{(*)}, \tag{9}$$

$$\mathbf{u}^{(k)} = \mathbf{u}^{(*)} - \frac{\alpha_k \Delta t}{\rho} \nabla p^{(k)}, \tag{10}$$

with the pressure correction term $p_{\text{corr}}$ calculated from the Poisson equation

$$\nabla \cdot \left( \frac{1}{\rho} \nabla p_{\text{corr}} \right) = \frac{1}{\alpha_k \Delta t} \nabla \cdot \mathbf{u}^{(*)}. \tag{11}$$

The fully parallelized BiCGStab algorithm with geometric multigrid preconditioning from the HYPRE library [29] is utilised to solve (11) most efficiently.

**Floating Body Dynamics**

The floating body is described implicitly in the computational domain using the signed distance function $\phi_s$. The function is generated from a STL geometry consisting of multiple non-connected triangles using a ray casting algorithm [30] to receive inside-outside information near the body and the same reinitialisation algorithm as for the free surface. Following the idea

in [31], the coupling conditions between the floating body and the fluid is accomplished through the definition of the source term $\mathbf{f}$ in (2). In the solid phase, this term is defined as

$$\mathbf{f} = \frac{\partial \mathbf{P}(\mathbf{u})}{\partial t} + \mathbf{P}(\mathbf{u}) \cdot \nabla \mathbf{P}(\mathbf{u}) + \frac{1}{\rho} \nabla p - \mathbf{g}, \tag{12}$$

with $\mathbf{P}(\mathbf{u})$ the projection of the velocity field obeying the rigid body velocity constraint. Using $H(\phi_s)$ for representing the transition between the definition of $\mathbf{f}$ in the fluid and solid phase and the derivation in [18], the term can be written as

$$\mathbf{f}^{(n+1)} = H(\Phi_s^{(n+1)}) \cdot \left( \frac{\mathbf{P}(\mathbf{u}^{(n+1)}) - \mathbf{u}^{(*)}}{\Delta t} \right). \tag{13}$$

A good approximation of the updated velocity field is $\mathbf{u}^{(*)}$ itself. Thus, the forcing term is added to the predicted velocity field before solving the correction steps using the definition

$$\mathbf{f}^{(*)} = H(\phi_s^{(*)}) \cdot \left( \frac{\mathbf{P}(\mathbf{u}^{(*)}) - \mathbf{u}^{(*)}}{\alpha_k \Delta t} \right), \tag{14}$$

with the projection

$$\mathbf{P}(\mathbf{u}^{(*)}) = \dot{\mathbf{x}}_{\mathbf{s}} + \boldsymbol{\omega}_{\mathbf{s}} \times \mathbf{r}. \tag{15}$$

Here, $\dot{\mathbf{x}}_{\mathbf{s}}$ are the three translational and $\boldsymbol{\omega}_{\mathbf{s}}$ the three rotational rigid body velocities defined in the inertial system of the Eulerian computational domain and $\mathbf{r}$ equals the distance vector between a point in the domain and the centre of gravity of the floating body. The rigid body velocities are determined from the conservation laws of translational and rotational impulse. A first-order system was derived in [32] which can be solved with the same Runge-Kutta scheme as described above. The fluid forces and momenta acting on the floating structure are calculated using

$$\mathbf{F_x} = \int_{\Omega} (-\mathbf{n}p + \rho \nu \mathbf{n}\tau) \, d\Omega(\mathbf{x}) = \sum_{i=1}^{N} (-\mathbf{n}p + \rho \nu \mathbf{n}\tau)_i \cdot \Delta \Omega_i,$$

$$\mathbf{M_x} = \int_{\Omega} \mathbf{r} \times (-\mathbf{n}p + \rho \nu \mathbf{n}\tau) \, d\Omega(\mathbf{x})$$
$$= \sum_{i=1}^{N} \mathbf{r}_i \times (-\mathbf{n}p + \rho \nu \mathbf{n}\tau)_i \cdot \Delta \Omega_i, \tag{16}$$

on the triangulated surface with trilinear interpolations of the fluid properties. Here, $N$ is the number of STL triangles, $\mathbf{n}$ is the corresponding surface normal vector and $\tau$ is the viscous stress tensor. External forces from mooring lines are also added directly to the dynamic equations to enable two way coupled simulations.

## Net Dynamics

The solidity ratio $S_n$ of a net describes the ratio of solid front area to the total area including the voids between the twines. It is approximated using

$$S_n = \frac{2d}{l} - \left(\frac{d}{l}\right)^2, \tag{17}$$

with $l$ the length and $d$ the diameter of the twines. Aquaculture nets consist of a very large number of small twines compared to the complete structural dimension and the length scale of the incoming waves. Thus, no conventional discretisation of the fluid domain around all details of the net structure is possible. In [17], a forcing method is proposed to approximate the correct boundary conditions at the fluid-structure interface. Here, a coupling term $\mathbf{S}$, which expresses the physical loss of fluid momentum due to the presence of the net leading to a pressure jump, is included in the momentum equations (see (2)). This term is calculated from the external forces acting on uniformly distributed Lagrangian points which follow the net. The uniformity is achieved by discretising the net surface into triangles with the same characteristic length as the surrounding fluid cells. The points are then defined in the geometrical centres of all triangles as illustrated in Fig. 2.

The external force vector $\mathbf{s}$ at the Lagrangian point with position $\mathbf{x}_L = (x_L, y_L, z_L)$ and corresponding area $A_L$ is determined using an extended screen force model. Besides the gravity and buoyancy forces, this includes inertia as well as hydrodynamic drag and lift forces:

$$\mathbf{s}(\mathbf{x}_L) = (\mathbf{G}_L + \mathbf{I}_L + \mathbf{D}_L) \cdot A_L. \tag{18}$$

The gravitational force $\mathbf{G}$ is approximated from the weight of the occupied net surface $A_L$. Further, the inertia force $\mathbf{I}_L$ is calculated as

$$\mathbf{I}_L = m_{a,L} \left(\mathbf{a_f} + \operatorname{diag}(n_x, n_y, n_z)\, \mathbf{a}_{\mathrm{rel}}\right)_L, \tag{19}$$

with $m_{a,L}$ the added mass, $\mathbf{n}_L$ the unit normal vector of $A_L$, $\mathbf{a}_{f,L}$ the fluid acceleration at $\mathbf{x}_L$ and $\mathbf{a}_{\mathrm{rel},L}$ the relative acceleration vector between fluid and structure. The added mass is thereby assumed to equal the mass of the water volume displaced by the solid cylindrical twines in $A_L$. As can be seen from (19), it is only applied in the direction of $\mathbf{n}_L$. The hydrodynamic drag and lift force $\mathbf{D}_L$ is given as

$$\mathbf{D}_L = \frac{\rho}{2} u_{\mathrm{rel},L}^2 \cdot (c_d \mathbf{n}_d + c_l \mathbf{n}_l)_L, \tag{20}$$

with $\mathbf{n}_d$ the normal and $\mathbf{n}_l$ the tangential direction of the relative vector $\mathbf{u}_{\mathrm{rel},L}$ between fluid and solid velocity. Further details about the calculation of (20) can be found in [17]. The forces are finally distributed on the fluid cell points $\mathbf{x}_e = (x_e, y_e, z_e)$ using

$$\mathbf{S}(\mathbf{x}_e) = \sum_{L=1}^{L_e} \frac{\mathbf{s}(\mathbf{x}_L)}{\Delta V}\, K\left(\frac{x_e - x_L}{\Delta x}\right)\, K\left(\frac{y_e - y_L}{\Delta y}\right)\, K\left(\frac{z_e - z_L}{\Delta z}\right), \tag{21}$$

with $L_e$ the number of Lagrangian points within a defined kernel $K$ around $\mathbf{x}_e$ and $\Delta V = \Delta x \Delta y \Delta z$.
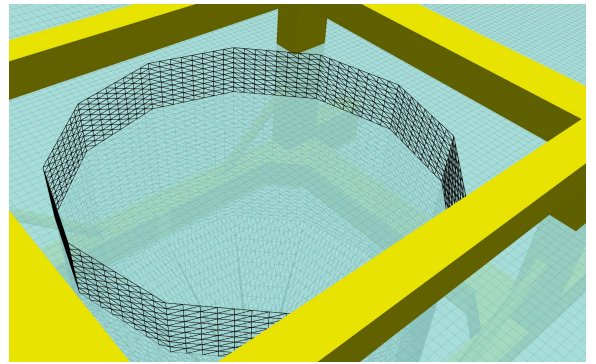


**FIGURE 2**: Illustration of the discretised net for the two-way coupling to the fluid solution. Each black triangle holds one Lagrangian point representing the portion of the net. The grey lines on the blue surface represent the fluid cells around the net. The solid floating body is shown in yellow.

In [19], an implicit method for solving the structural dynamics of nets was proposed. However, offshore aquaculture structures are typically equipped with relatively stiff nets with negligible deformations. It could be shown in [18] that it is appropriate to assume that the net moves with the rigid floating structure in this case. Thus, the Lagrangian points are updated in each time step using the translational and rotational velocities of the floating body. A two-way coupled approach is chosen by adding the forces acting on the net as external forces to the rigid body dynamics equations. The interaction of the net and fluid is accomplished through the described coupling term (21).

## RESULTS

Extensive validation of the proposed numerical framework has been presented for floating body motion in waves, the fluid-net coupling in current and waves as well as the coupling of the floating body and the net in [17–19]. In the following, the rigid

floating structure Havfarm 2 from Nordlaks and NSK Ship Design [33] is utilised to study the effects of wave and current on OOA structures. The 1 : 40 model test results obtained from measurements in the ocean basin of SINTEF Ocean in Trondheim, Norway, are considered for validation purposes.

As can be seen from Fig. 3, multiple rectangular beams compose the main structure which is approximately 7.5 m long, 1.6 m wide and 1.1 m high. The design draft used in this study is 0.8 m. Between the longitudinal beams, four equally sized box-shaped spaces are formed. In each space, a net is embedded in the form of the frustum of a pyramid and tightly fastened to the frame. At the lower end of the nets, a pyramid-shaped net is attached to increase the enclosed volume. All nets have a solidity of 0.22. In contrast to previous research [18], the deformation of the nets is neglected due to its minor influence on the motion of these type of OOA structures. The validity of this assumption is confirmed below.
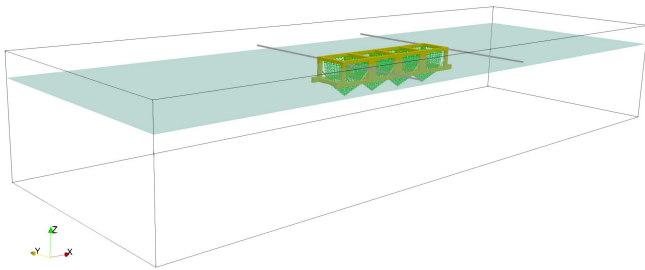


**FIGURE 3**: Rigid floating OOA structure in a numerical wave tank. The structure is shown in yellow, the nets in green and the mooring lines in grey. The free surface is indicated in blue.
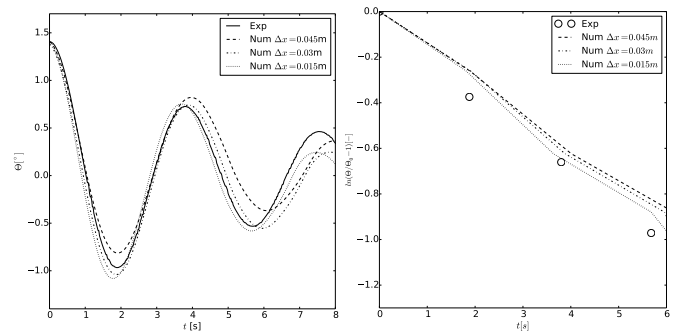
## Decay Tests

A grid convergence study is conducted using the decay tests in pitch and heave. A refinement box with a uniform cell size of $\Delta x = \Delta y = \Delta z = 0.045, 0.03$ and $0.015$ m is placed in a rectangular domain of $15 \times 10 \times 10$ m. The chosen domain size is justified by placing numerical beaches at all domain boundaries to absorb the energy induced by the structural motion. The water height is 8 m. The cell size is gradually coarsened towards the domain boundaries with a ratio of 1.1. The OOA structure including the attached nets is placed in the centre of the refinement box with an initial displacement of $\Delta z = 0.09$ m for the heave decay test and $\Delta \Theta = 1.4°$ for the pitch decay test. Small displacements of the other degrees of freedom in the model tests are respected in the simulations as well.

The time series of the decay tests are compared to the measurements in Fig. 4. On the coarsest grid, a too-large heave frequency and a relatively large peak deviation are predicted (see Fig. 4a). A cell size of 0.03 m around the structure improves the results, especially for the first peaks. Further convergence of the

solution towards the experimental data is seen for the finest grid size. In Fig. 4b, the decay rate is plotted as the damping ratio over time. The numerical solution can replicate the measured damping on all grids. Similarly, the time series and decay rate for the simulated pitch decay test is presented in the Figs. 4c-4d. The pitch frequency converges towards the reported value with decreasing cell size. The first three peaks are captured well with the two finer grids, whereas an under-prediction is present at the last peak. A further refinement might improve the results, but it should also be noticed that the angles itself are already very small in magnitude. Hence, small deviations in the setup can have significant effects on the results. As for the heave decay test, the decay rate is predicted well by the numerical model, and the convergence of the results with increasing grid size is visible. Based on these results, a cell size of 0.03 m is chosen around the structure for the analyses below.
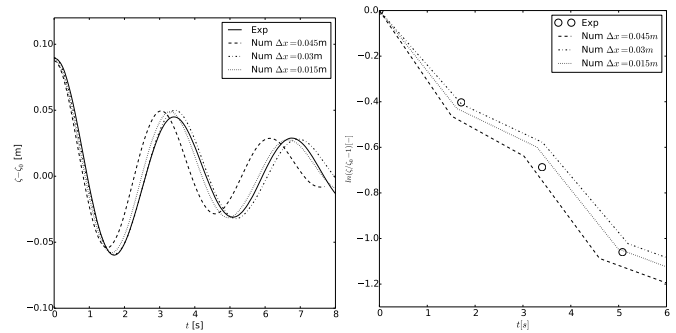


(a) Time series of the heave decay test. (b) Decay rate for the heave decay test.



(c) Time series of the pitch decay test. (d) Decay rate for the pitch decay test.

**FIGURE 4**: Comparison of the numerical and experimental results for the decay tests of the OOA structure.

## Current

The current flow around the OOA structure is investigated next. The length of the numerical domain of the decay test is doubled in $x$- and $y$-direction for this purpose. At the inlet, a constant

velocity of 0.83 m/s and 1.0 m/s is prescribed. The side boundaries are modelled as walls, and a free outflow boundary condition is placed at the outlet. The influence of the flow direction is investigated by rotating the structure gradually. Thus, angles of attack $\alpha$ of $0, 15, 45$ and $90°$ are considered. Physical model tests were performed for the first three angles of attack. The structure was fixed by a stiff mooring system during the experiments. In the simulations, all degrees of freedom are prevented to replicate this setup. The velocities in $x$ and $y$ direction are measured in the centre of each cage 0.1 m below the free surface over 30 s. The mean values are then computed and compared to the model test results in the Figs. 5-6. In x-direction, the velocities are presented as the velocity reduction factors $U_r = 1 - U/U_\infty$ which is a common quantity in aquaculture applications. The physically measured velocity time series showed large velocity oscillations for which reason the experimental values are plotted as bars indicating the variation of one standard deviation around the mean value.
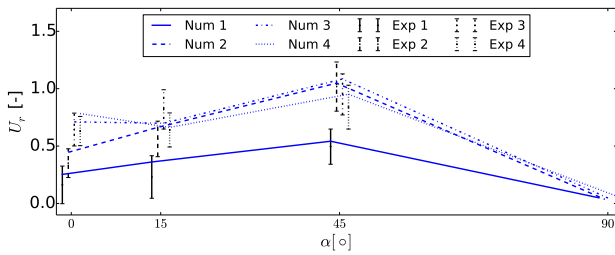


(a) Velocity reduction factors over $\alpha$ for $U_\infty = 0.83$ m/s.
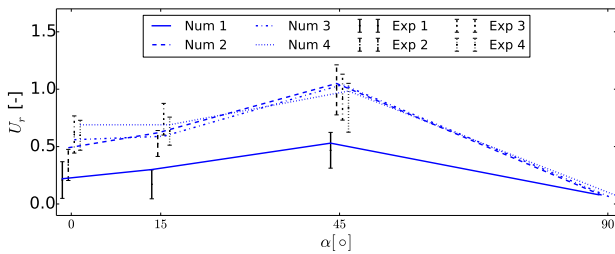


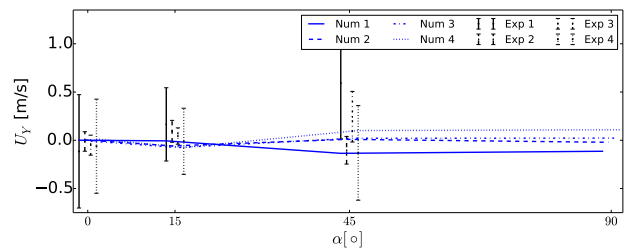(b) Velocity reduction factors over $\alpha$ for $U_\infty = 1.0$ m/s.

**FIGURE 5**: Mean velocity reduction factors inside the net cages for different inflow velocities $U_\infty$ and angles of attack. The numbers in the legend indicate the cage number with 1 representing the cage in the fore. The vertical bars indicate the model test results in terms of one standard deviation around the mean value.

In Fig. 5, the velocity reduction factors are compared. It is first noticed that the factors are similar for the two inflow velocities. This is in accordance with the results in [17] for the flow through a rigid net panel. After the flow passes the front part of the net, the fluid velocity reduces by approximately 20% for

$\alpha = 0°$. The velocity in the first net further decreases for angles of attack up to $45°$ because the recirculation zone behind the rigid parts of the structure is turned into the centric part of the net (see Fig. 7a). The reduction factors generally increase with each additionally past net if no heading angle is present. At the heading angles of 15 and $45°$, this changes significantly as the factor in the aft net of the body is smaller than in the central nets 2 and 3. This is probably caused by a relatively undisturbed inflow at the last net compared to the more chaotic flow patterns in front of the central nets arising from the fluid-structure interaction at the front net. This effect is however rather small compared to the observation that the velocity reduction generally reduces again for heading angles larger than $45°$. It is caused by the fact that with increasing angle, the flow is passing fewer net surfaces which would cause additional velocity reductions (compare Fig. 7b). At $90°$, the velocity reduction factors are similar in all nets (about 0.08) due to the undisturbed inflow sidewards. All described phenomena are well captured by the numerical model because the predicted velocity reduction factors are within the chosen range of measured results.
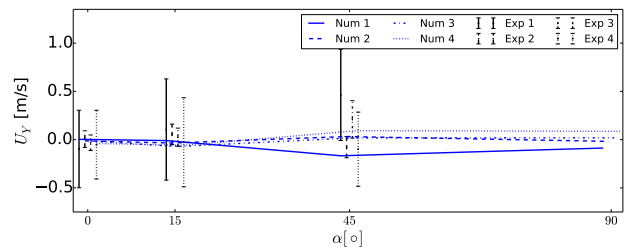


(a) Velocities in y-direction over $\alpha$ for $U_\infty = 0.83$ m/s.



(b) Velocities in y-direction over $\alpha$ for $U_\infty = 1.0$ m/s.

**FIGURE 6**: Mean velocities in y-direction inside the net cages for different inflow velocities $U_\infty$ and angles of attack. See Fig. 5 for further explanations.

In contrast to the velocities in x-direction, the mean y-velocities in Fig. 6 are generally smaller and oscillate more. This is again caused by the recirculation zones behind each beam interacting the flow in the net cages. This effect is largest for the cages in the front and aft of the structure and $\alpha = 0$ and $45°$ be-

Copyright © 2021 by ASME

cause, at these locations, the inflow velocity is relatively large. This might cause stronger fluctuations of the turbulent recirculation zones. In contrast, the fluctuations in y-direction are small in the central cages due to the fluid being blocked by the structure and nets in front of them. It is finally noticed that for $\alpha = 90°$, both the y-velocities in the outer nets and the velocities in the central nets are symmetrical. Here, the velocities in the outer nets tend to be larger because of the asymmetrical frame enclosing these nets compared to the symmetrical configuration around the inner nets.
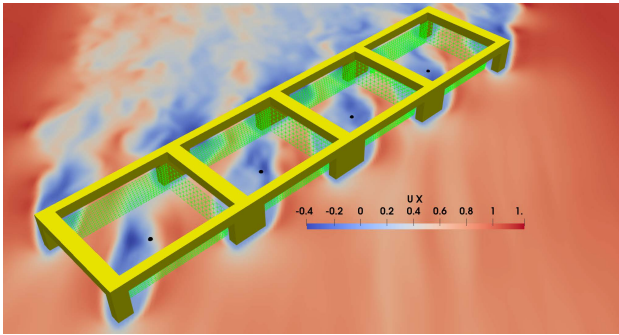


(a) $\alpha = 45°$.
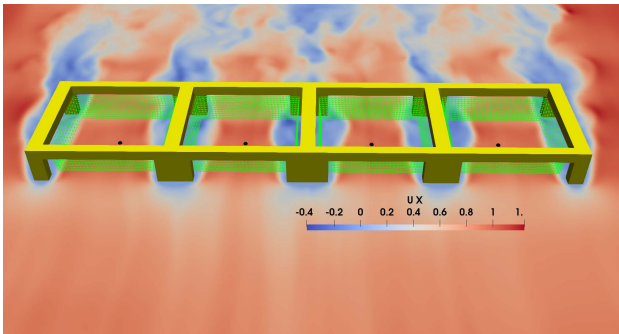


(b) $\alpha = 90°$.

**FIGURE 7**: X-velocity profiles in the plane through $z = 7.8$ m for two different heading angles and $U_\infty = 1.0$ m/s. Incident flow from the bottom. The black dots indicate the probe points.

## Waves

Next, the dynamic response of the OOA structure in waves is investigated. Two regular waves with a height of $H = 0.1125$ m and the frequencies of $f = 0.421$ Hz (wave 1) and $f = 0.294$ Hz (wave 2) were considered in the experiment. A numerical wave tank is established to reproduce the physical setup (see Fig. 3). At the inlet, a relaxation zone [24] is defined to generate the waves as second-order Stokes waves. A numerical beach at the end of the tank damps the waves such that reflections can be avoided. The structure is placed in the middle of the tank with heading

angles between 0 and 90°. Four mooring lines are horizontally attached to the sides of the structure to keep the structure in the centre of the tank. The lines are modelled as springs with predefined pre-tension in accordance with the experimental setup.

**TABLE 1**: Measured meain frequencies for the motion of the OOA structure in waves. G1 and G3 are the two wave gauges. All measures in Hz.

| $H[m]$ | $f$ | $\alpha$ | $G1$ | $G3$ | $Surge$ | $Heave$ | $Roll$ | $Pitch$ | $Yaw$ |
|---|---|---|---|---|---|---|---|---|---|
| 0.1125 | 0.421 | 0 | 0.424 | 0.424 | – | 0.424 | – | 0.425 | – |
| 0.1125 | 0.421 | 15 | 0.424 | 0.424 | – | 0.425 | 0.425 | 0.424 | 0.425 |
| 0.1125 | 0.421 | 45 | 0.424 | 0.424 | 0.425 | 0.425 | 0.425 | 0.425 | 0.424 |
| 0.1125 | 0.294 | 0 | 0.291 | 0.291 | 0.291 | 0.291 | – | 0.291 | – |
| 0.1125 | 0.294 | 15 | 0.291 | 0.292 | 0.294 | 0.291 | 0.293 | 0.291 | 0.291 |
| 0.1125 | 0.294 | 45 | 0.292 | 0.291 | 0.293 | 0.291 | 0.294 | 0.293 | 0.294 |

**TABLE 2**: Numerically calculated main frequencies for the motion of the OOA structure in waves. G1 and G3 are the two wave gauges. All measures in Hz.

| $H[m]$ | $f$ | $\alpha$ | $G1$ | $G3$ | $Surge$ | $Heave$ | $Roll$ | $Pitch$ | $Yaw$ |
|---|---|---|---|---|---|---|---|---|---|
| 0.1125 | 0.421 | 0 | 0.422 | 0.422 | – | 0.419 | – | 0.421 | – |
| 0.1125 | 0.421 | 15 | 0.422 | 0.422 | – | 0.424 | 0.421 | 0.422 | 0.422 |
| 0.1125 | 0.421 | 45 | 0.421 | 0.422 | 0.421 | 0.420 | 0.421 | 0.420 | 0.422 |
| 0.1125 | 0.294 | 0 | 0.293 | 0.294 | 0.293 | 0.294 | – | 0.294 | – |
| 0.1125 | 0.294 | 15 | 0.293 | 0.294 | 0.295 | 0.294 | 0.292 | 0.293 | 0.295 |
| 0.1125 | 0.294 | 45 | 0.293 | 0.294 | 0.293 | 0.294 | 0.293 | 0.294 | 0.294 |

At first, the waves are validated at two different wave gauges. G1 is located 1.5 m in front of the structure and G3 is located 1.5 besides the centre of the structure. The measured frequencies are summarised in the Tabs. 1 and 2, and the amplitudes can be found in Fig. 8a. The model tests measure a minor increase of the frequency for the short wave and a minor decrease in the frequency for the long wave. In contrast, the simulation predicts wave frequencies very close to the input signal. The maximum deviation is less than 1%. Similar accuracy is achieved for the amplitudes except for the short wave at G3 were an under-prediction of about 7% is present.

The translational motions surge and heave, as well as the rotational motions around all three axes, are considered next. The

frequencies can be found in Tabs. 1 and 2, whereas the Figs. 8b and 8c compare the amplitudes obtained from a FFT analysis of the time series signal. The simulated results show motion frequencies close to the wave frequency and the experimental results. Further, the heave and surge amplitudes are larger for the longer wave which has a wavelength of twice the structural length. Generally, a good agreement between experimental and numerical results can be stated for the translational motions with deviations of less than 15% for all cases.
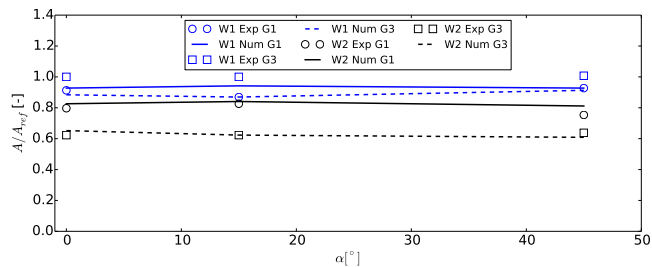


(a) Wave amplitude at the two wave gauges.
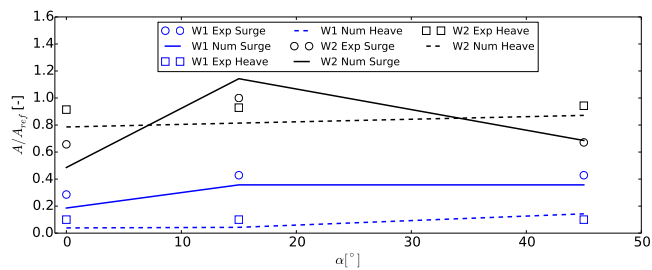


(b) Amplitudes of the translational motions.
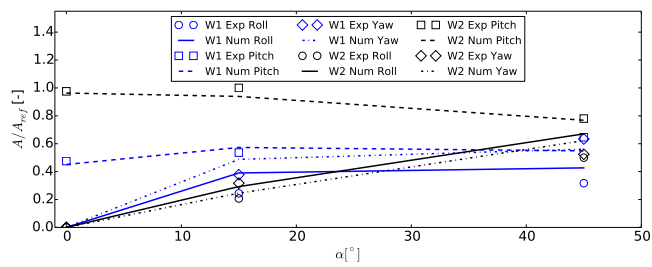


(c) Amplitudes of the rotational motions.

**FIGURE 8**: Numerical and experimental results for the mean wave amplitudes and mean response amplitudes for different heading angles $\alpha$. The amplitudes are calculated using a FFT and normalised with the largest measured amplitude. The two wave inputs are indicated in blue (wave 1) and black (wave 2).

The amplitudes of the rotational motions are presented in Fig. 8c. The largest rotations are observed around the y-axis (pitch) with up to 0.8°. Pitch is also larger in the long wave

because the wave crest reaches the front of the structure while at the same time a wave trough is present at the aft. In comparison, two wave crests are at both ends of the structure in the shorter wave with a wavelength similar to the structure (compare Fig. 9). The pitch motion tends to decrease with increasing heading angle due to the shortening of the structural dimensions in wave direction. In contrast, the rotations around the body fixed x- and z-axis increase with $\alpha$ due to the same reason. In general, the numerical model agrees well with the experiments at small heading angles as the deviations are below 5%. Larger differences are observed for the roll motion at $\alpha = 45\%$ (about 15%) which might be caused by a slightly different attachment position of the mooring lines in the experiments.
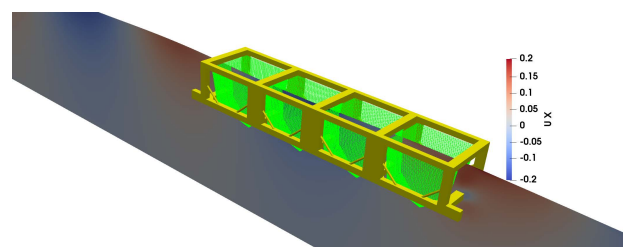


(a) Short wave (wave 1).
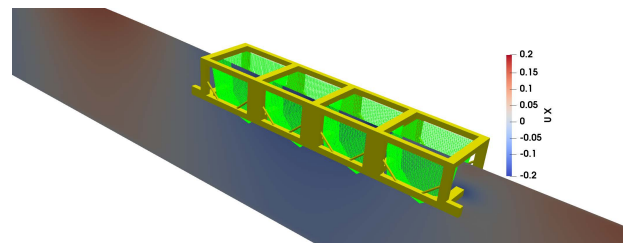


(b) Long wave (wave 2).

**FIGURE 9**: X-velocity profiles under the free surface in the plane through the centre of the structure for $\alpha = 15°$ and the two different wave inputs. The waves propagate from the left to the right.

Finally, the mean force amplitudes of the four different nets are analysed in Fig. 10. No experimental data are given for this property. If no heading angle is present, the forces are largest in x-direction whereas the forces in y-direction are close to zero. Despite the circular motion of the fluid particles in the given waves, the forces in z-direction are smaller due to the small bottom surface of the net compared to the vertical surfaces. Also, the forces are larger in the short wave than in the long wave. This might be due to the smaller structural motions in wave 1 leading to a more direct inflow into the cages. The force magnitudes tend to decrease with increasing heading angles due to a stronger blockage effect through the rigid structure. It is further noticed that no clear pattern of the force direction and magnitude

Copyright © 2021 by ASME

can be found for the different net cage positions. This indicates that the structural motion, including its blockage effects at different heading angles, has an important effect on the expected net forces, whereas the shielding effect of the nets plays an insignificant role for the nets in the aft of the OOA structure.
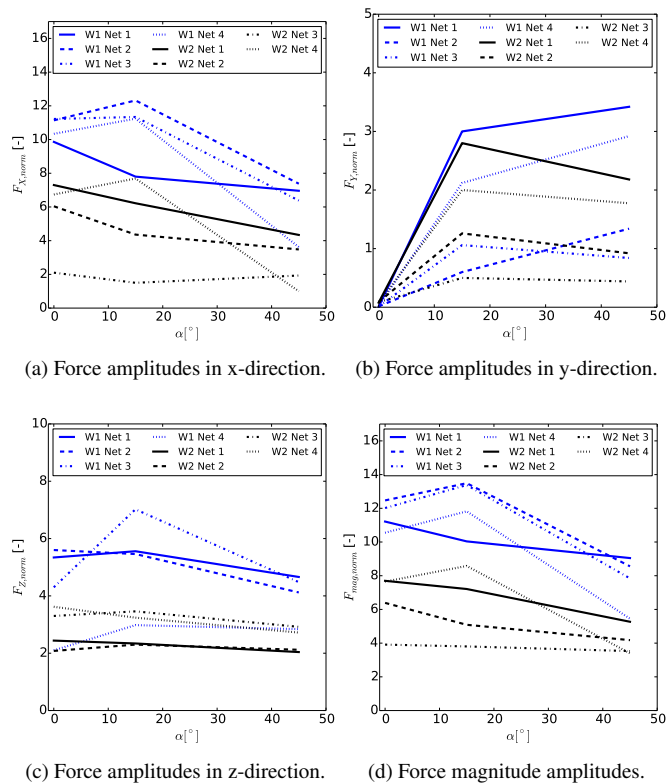


(a) Force amplitudes in x-direction.

(b) Force amplitudes in y-direction.

(c) Force amplitudes in z-direction.

(d) Force magnitude amplitudes.

**FIGURE 10**: Numerical results for the mean net force amplitudes for different heading angles $\alpha$. The results are normalised with the smallest force in x-direction at net 4.

## CONCLUSION

In this paper, a CFD approach for the simulation of OOA structures in waves is presented. The model solves the Navier-Stokes equations for an incompressible two-phase fluid with additional source terms to account for the floating rigid structure and the shielding effects of the net. Hence, two-way coupled simulations of all involved parts are enabled. It is proposed that the net in OOA structures can be modelled as a rigid surface moving with the frame structure due to its high stiffness. The presented study indicates the validity of this assumption. Thus, it would be straightforward to apply this approach to deforming nets as shown in [19]. The numerical model was applied to the rigid floating aquaculture facility Havfarm 2 in current and waves.

The correct representation of the structural motion in the fluid was successfully validated using decay tests in heave and pitch. In current, the velocities inside the cages are mainly influenced by the heading angle of the structure. For angles between 0 and 90°, complex flow patterns are observed. Angles of 90° result in smooth flow patterns and the highest velocities inside all cages. In practice, this would be the ideal flow condition as it ensures the optimal circulation of oxygen and removal of pollution. The investigation of the motion in waves reveals relatively large translational motions in long waves and relatively large rotational motions in waves with lengths equal to the length of the structure. Besides, it could be shown that the forces on the net cages are rather influenced by the motion and location of the structure than by the shielding effect of the cages. This is in contrast to the observations in current.

## ACKNOWLEDGEMENT

## REFERENCES

[1] Ferreira, J., Saurel, J., Lencart e Silva, J., Nunes, J., and Vazquez, F., 2014. "Modelling of interactions between inshore and offshore aquaculture". *Aquaculture*, pp. 154–164.

[2] Patursson, Ø., Swift, M. R., Tsukrov, I., Simonsen, K., Baldwin, K., Fredriksson, D., and Celikkol, B., 2010. "Development of a porous media model with application to flow through and around a net panel". *Ocean Engineering*, **37**, pp. 314–324.

[3] Bi, C.-W., Zhao, Y.-P., Dong, G.-H., Xu, T.-J., and Gui, F.-K., 2013. "Experimental investigation of the reduction in flow velocity downstream from a fishing net". *Aquaculture Engineering*, **57**, pp. 71–81.

[4] Føre, H., Endresen, P., Norvik, C., and Lader, P., 2020. "Loads on net panels with different solidities". *ASME 2020 39th International Conference on Ocean, Offshore and Arctic Engineering*.

[5] Bi, C.-W., Zhao, Y.-P., Dong, G.-H., Xu, T.-J., and Gui, F.-K., 2014. "Numerical simulation of the interaction between flow and flexible nets". *J. Fluids Struct.*, **45**, pp. 180–201.

[6] Lader, P. F., and Enerhaug, B., 2005. "Experimental investigation of forces and geometry of a net cage in uni-

form flow". *IEEE Journal of Oceanic Engineering,* **30**(1), pp. 79–84.

[7] Lader, P., Jensen, A., Sveen, J. K., Fredheim, A., Enerhaug, B., and Fredriksson, D., 2007. "Experimental investigation of wave forces on net structures". *Applied Ocean Research,* **29**(3), pp. 112–127.

[8] Kristiansen, T., and Faltinsen, O. M., 2015. "Experimental and numerical study of an aquaculture net cage with floater in waves and current". *Journal of Fluids and Structures,* **54**, pp. 1–26.

[9] Shen, Y., Greco, M., Faltinsen, O., and Nygaard, I., 2018. "Numerical and experimental investigations on mooring loads of a marine fish farm in waves and current". *Journal of Fluids and Structures,* **79**, p. 115–136.

[10] Fredriksson, D., Swift, M., Eroshkin, O., Tsukrov, I., Irish, J., and Celikkol, B., 2005. "Moored fish cage dynamics in waves and currents". *IEEE Journal of Oceanic Engineering, 30(1)*, pp. 28–36.

[11] Fredriksson, D., Swift, M., Irish, J., Tsukrov, I., and Celikkol, B., 2003. "Fish cage and mooring system dynamics using physical and numerical models with field measurements". *Aquacultural Engineering,* **27**, pp. 117–146.

[12] Li, L., Jiang, Z., Vangdal Høiland, A., and Chen Ong, M., 2018. "Numerical Analysis of a Vessel- Shaped Offshore Fish Farm". *Journal of Offshore Mechanics and Arctic Engineering,* **140**. doi: 10.1115/1.4039131.

[13] Chen, H., and Christensen, E., 2018. "Simulating the hydrodynamic response of a floater net system in current and waves". *J. Fluids Struct.,* **79**, pp. 50–75.

[14] Chen, H., and Christensen, E., 2016. "Investigations on the porous resistance coefficients for fishing net structures". *J. Fluids Struct.,* **65**, pp. 76–107.

[15] Chen, H., and Christensen, E., 2017. "Development of a numerical model for fluid-structure interaction analysis of flow through and around an aquaculture net cage". *Ocean Engineering,* **142**, pp. 597–615.

[16] Zhao, Y.-P., Bi, C.-W., Liu, Y.-X., Dong, G.-H., and Gui, F.-K., 2014. "Numerical Simulation of Interaction Between Waves and Net Panel Using Porous Media Model". *Engineering Applications of Computational Fluid Mechanics,* **8**(1), pp. 116–126.

[17] Martin, T., Kamath, A., and Bihs, H., 2020. "A Lagrangian approach for the coupled simulation of fixed net structures in a Eulerian fluid model". *Journal of Fluids and Structures, (94)*. doi: 10.1016/j.jfluidstructs.2020.102962.

[18] Martin, T., Tsarau, A., and Bihs, H., 2020. "A numerical framework for modelling the dynamics of open ocean aquaculture structures in viscous fluids". *Applied Ocean Research,* ***In Press***. doi: 10.1016/j.apor.2020.102410.

[19] Martin, T., and Bihs, H., 2021. "A non-linear implicit approach for modelling the dynamics of porous tensile structures interacting with fluids". *Journal of Fluids and Structures,* **Volume 100**. doi: 10.1016/j.jfluidstructs.2020.103168.

[20] Peskin, C. S., 1977. "Numerical analysis of blood flow in the heart". *Journal of Computational Physics,* **25 (3)**, p. 220–252.

[21] Uhlmann, M., 2005. "An immersed boundary method with direct forcing for the simulation of particulate flows". *Journal of Computational Physics,* **209**, pp. 448–476.

[22] Osher, S., and Sethian, J., 1988. "Fronts propagating with curvature-dependent speed: Algorithms based on Hamilton-Jacobi formulations". *Journal of Computational Physics,* **79**, pp. 12–49.

[23] Sussman, M., Smereka, P., and Osher, S., 1994. "A level set approach for computing solutions to incompressible two-phase flow". *Journal of Computational Physics,* **114**, pp. 146–159.

[24] Bihs, H., Kamath, A., Alagan Chella, M., Aggarwal, A., and Arntsen, Ø. A., 2016. "A new level set numerical wave tank with improved density interpolation for complex wave hydrodynamics". *Computers & Fluids,* **140**, pp. 191–208.

[25] Jiang, G., and Peng, D., 2000. "Weighted ENO schemes for Hamilton Jacobi equations". *SIAM Journal of Scientific Computing,* **21**, pp. 2126–2143.

[26] Jiang, G., and Shu, C., 1996. "Efficient implementation of weighted ENO schemes". *Journal of Computational Physics,* **126(1)**, pp. 202–228.

[27] Timmermans, L., Minev, P., and Van De Vosse, F., 1996. "An approximate projection scheme for incompressible flow using spectral elements". *International Journal for Numerical Methods in Fluid,* **22**, pp. 673–688.

[28] Shu, C., and Osher, S., 1988. "Efficient implementation of essentially non-oscillatory shock-capturing schemes". *Journal of Computational Physics,* **77(2)**, pp. 439–471.

[29] van der Vorst, H., 1992. "BiCGStab: A fast and smoothly converging variant of Bi-CG for the solution of nonsymmetric linear systems". *SIAM Journal of Scientific Computing,* **13**, pp. 631–644.

[30] Bihs, H., Kamath, A., Chella, M. A., and Pakozdi, C., 2017. "Complex geometry handling for a cartesian grid based solver". *MekIT, 17-Ninth national conference on Computational Mechanics*.

[31] Yang, L., 2018. "One-fluid formulation for fluid–structure interaction with free surface". *Comput. Methods Appl. Mech. Engrg.,* **332**, pp. 102–135.

[32] Martin, T., Kamath, A., and Bihs, H., 2020. "Accurate modeling of the interaction of constrained floating structures and complex free surfaces using a new quasistatic mooring model". *International Journal for Numerical Methods in Fluids*. doi: 10.1002/fld.4894.

[33] Nordlaks. https://www.nordlaks.no/havfarm/om-havfarm-prosjektet. accessed 21.12.2020.